Laser ultrasonics in a multilayer structure: Semi-analytic model and simulated examples

R. Hodé, M. Ducousso, N. Cuvillier, V. Gusev, V. Tournat, S. Raetz, et al.

Laser ultrasonics in a multilayer structure: Semi-analytic model and simulated examples

R. Hodé,[1,a)] M. Ducousso,[2,b)] N. Cuvillier,[2,c)] V. Gusev,[1,d)] V. Tournat,[1,e)] and S. Raetz[1,f)]

[1]*Laboratoire d'Acoustique de l'Université du Mans (LAUM), UMR 6613, Institut d'Acoustique–Graduate School (IA-GS), CNRS, Le Mans Université, France*

[2]*Safran Tech, Rue des Jeunes Bois-Châteaufort, 78772 Magny-les-Hameaux, France*

ABSTRACT:

Laser-generated elastic waves have been the subject of numerous experimental, theoretical, and numerical studies to describe the opto-acoustic generation process, involving electromagnetic, thermal, and elastic fields and their couplings in matter. Among the numerical methods for solving this multiphysical problem, the semi-analytic approach is one of the most relevant for obtaining fast and accurate results, when analytic solutions exist. In this paper, a multilayer model is proposed to successively solve electromagnetic, thermal, and elastodynamic problems. The optical penetration of the laser line source, as well as thermal conduction and convection, are accounted for. Optical, thermal, and mechanical coupling conditions are considered between the upper and lower media of the multilayer. The simulation of laser-generated ultrasounds in multilayer structures is of interest for the development of nondestructive evaluation methods of complex structures, such as bonded assemblies in aeronautics [as discussed in Hodé *et al.*, J. Acoust. Soc. Am. **150**, 2076 (2021)]. The developed PYTHON code is provided for free at https://doi.org/10.5281/zenodo.4301720.
© 2021 Acoustical Society of America. https://doi.org/10.1121/10.0005974

I. INTRODUCTION

Laser-generated ultrasounds are of great interest for the nondestructive evaluation (NDE) of material and mechanical structures. In aeronautics, the non-contact feature of this laser inspection is a significant advantage over more conventional techniques such as piezoelectric transducers with coupling agent. Furthermore, the opto-acoustic generation in the thermoelastic regime[1,2] ensures the integrity of the structure after the laser pulse impact. In the literature, laser-generated elastic waves[3] in metals were experimentally observed in the thermoelastic regime by Scruby *et al.*[4] Then, the theoretical basis was formulated by Rose,[5] where the thermoelastic generation at the surface of a half-space was represented by a point-source, called the surface center of expansion (SCOE) by the author.

Following this seminal work, simulations of laser-generated ultrasounds in elastic media have been carried out using analytic or semi-analytic approaches. Dubois *et al.*[6] reported an analytic one-dimensional model taking the optical penetration effect into account. Coulette *et al.*[7] simulated elastic waves propagation in a bilayer of cylindrical

symmetry with a semi-analytic model. The structure was composed of two orthotropic and homogeneous plates which were perfectly coupled [continuity of displacements and elastic forces (stresses) at the interface between the two media]. The optical reflection at the interface and the thermal diffusion were neglected in their numerical calculations. Murray *et al.*[8] used a similar approach based on the Hankel and Laplace transforms to simulate elastic waves propagating in an isotropic plate perfectly coupled to a semi-infinite medium. Cheng *et al.*[9] extended the work of Murray *et al.*[8] to isotropic layered plates, using the transfer matrix method.[10] The structure was illuminated by an axisymmetric laser source, but the optical penetration and the thermal diffusion were not considered. Audoin and Guilbaud,[11] Meri,[12] Perton,[13] and Raetz[14] gradually developed a semi-analytic model, based on the Fourier transform, to simulate acoustic waves generated by a laser line source. Specifically, Perton[13] modeled a bilayer structure, composed of two orthotropic, homogeneous, and viscoelastic plates perfectly coupled, with the plane strain hypothesis. The transmission of electromagnetic waves in the two media were considered, but reflections at the interface and the rear surface of the bilayer were neglected. Thermal conduction was also accounted for by considering three thermal waves: two propagating in the first medium and only one in the second (reflections at the rear surface were neglected).

Other numerical approaches such as finite element[15–17] or finite difference methods[18,19] have also been used to simulate laser-generated ultrasounds in the thermoelastic regime. These numerical methods are well suited for the

a)Electronic mail: romainod@gmail.com, ORCID: 0000-0001-7883-9621.
b)Electronic mail: mathieu.ducousso@safrangroup.com, ORCID: 0000-0002-4014-6747.
c)ORCID: 0000-0002-1577-3458.
d)ORCID: 0000-0002-2394-7892.
e)ORCID: 0000-0003-4497-5742.
f)Electronic mail: samuel.raetz@univ-lemans.fr, ORCID: 0000-0003-3683-8764.

simulation of elastic waves in media with complex geometry. However, they require more computing power than semi-analytic calculations. This can be a drawback when numerous simulations have to be performed for inverse problem solving, for instance. Hence, when analytic solutions can be found for wave propagation in media with simple geometry, the semi-analytic approach is the most appropriate choice to obtain accurate results quickly.

In this paper, a semi-analytic model is described where electromagnetic (Sec. III), thermal (Sec. IV), and elastodynamic (Sec. V) problems are successively solved to obtain the displacement field in the upper and lower media of a multilayer structure. The geometry and the main assumptions about the optical, thermal, and mechanical properties of the layers are detailed in Sec. II. Numerical results are presented in Sec. VI to give examples of simulations that can be performed with this semi-analytic model.

II. GEOMETRY AND ASSUMPTIONS

The geometry of the multilayer structure is illustrated in Fig. 1. The multilayer is composed of two solid media I and II of thicknesses h_1 and h_2, respectively, and two semi-infinite media (0 and III), which are assumed to be air. The origin of the Cartesian coordinate system $(O, \mathbf{x}_1, \mathbf{x}_2)$ is located at the upper surface of medium I. Note that in the previous definition of the coordinate system and for the remainder, a bold letter stands for a vector. The layers are considered to be of infinite dimension in the $\mathbf{x}_2$ and $\mathbf{x}_3$-directions. The incident tilted laser line source is oriented along the $\mathbf{x}_3$-direction. Thus, the electromagnetic, thermal, and mechanical problems are solved in 2D. Sublayers, with

a total thickness of Δh, can be inserted between media I and II and are denoted by the uppercase letter "EM" in Fig. 1 for the electromagnetic problem, by "T" in Fig. 2 for the thermal problem, and by "M" in Fig. 3 for the mechanical problem. These sublayers will be taken into account later in the coupling conditions between media I and II. The main assumptions made for the optical, thermal, and mechanical properties of the layers are introduced below.

In Sec. III, all layers are assumed electromagnetically linear, isotropic, and homogeneous. This means that the dielectric constant ε and magnetic permeability μ are scalar quantities and not position dependent. The materials constituting the layers should therefore not be birefringent, or at least have a negligible birefringence. These constants are also assumed to be independent of the temperature but related to the angular frequency ω_0 of the assumed monochromatic electromagnetic field. Moreover, the electric and magnetic polarization fields are not taken into account. In addition, the electric charge density ρ_q is supposed to be zero. This is a valid assumption, especially for metals, because ρ_q decays exponentially with time (relaxation time on the order of 10^{-18} s; see p. 736 of Ref. 20). This hypothesis implies that the divergence of the electric displacement is zero, $\nabla \cdot \mathbf{D} = 0$, as is the convection current density: $\mathbf{j}_v = \mathbf{0}$.

In Sec. IV, the thermal properties of the solid media are assumed linear, homogeneous, temperature independent, and orthotropic, with $\mathbf{x}_1$ and $\mathbf{x}_2$ as principal axes. Thermal conduction in the solid layers and convection phenomena at the upper surface of medium I (at $x_1 = 0$) and the lower surface of medium II (at $x_1 = H$ with $H = h_1 + \Delta h + h_2$) are considered.

In Sec. V, the mechanical properties of solid media are assumed linear, homogeneous, temperature independent, viscoelastic, and orthotropic, with $\mathbf{x}_1$ and $\mathbf{x}_2$ as principal axes. Elastic waves propagating in semi-infinite media (0 and III) are neglected. Furthermore, the plane strain
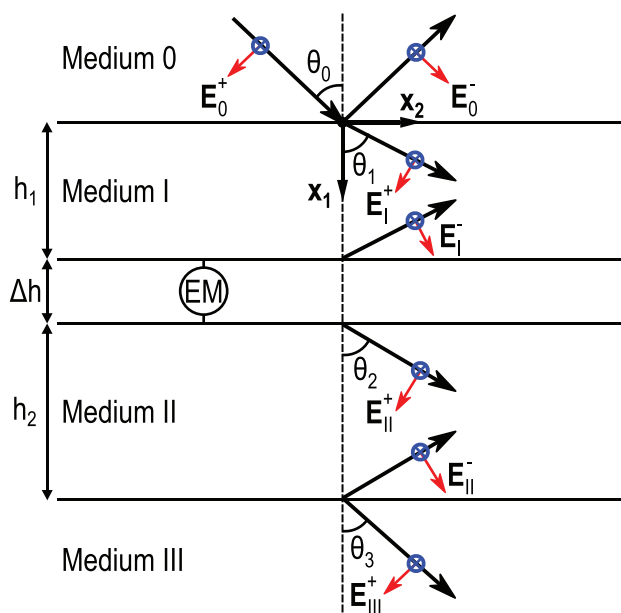

FIG. 1. (Color online) The geometry of the multilayer structure is represented with the two semi-infinite media (0 and III) and the media I and II of thicknesses h_1 and h_2, respectively. The uppercase letters "EM" symbolize the sublayers, with a total thickness of Δh, that can be inserted between media I and II. The black arrows represent the $\mathbf{k}$-wave vectors, and the red (blue) arrows indicate the electric vectors $\mathbf{E}$ (magnetic vectors $\mathbf{H}$).

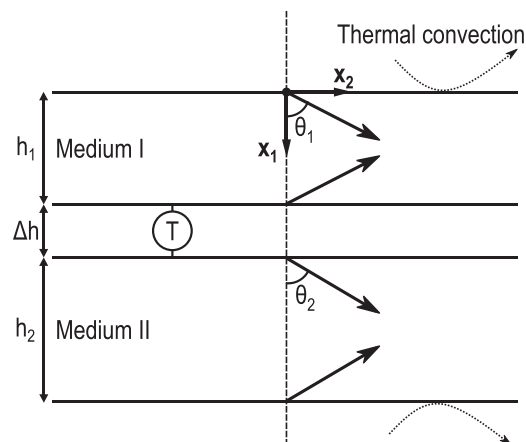FIG. 2. Illustration of the multilayer structure used to solve the thermal diffusion problem. The uppercase letter "T" denotes the sublayers that can be inserted between media I and II. The black arrows represent the wave vectors of the thermal waves propagating in the $\pm x_1$-direction. The two dotted arrows indicate the thermal convection at the upper surface of medium I and the lower surface of medium II.
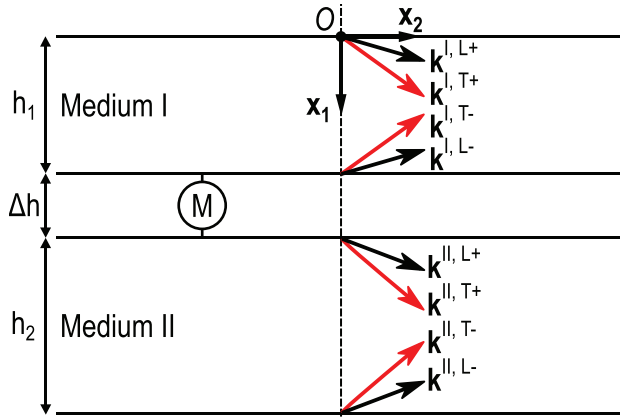
FIG. 3. (Color online) Representation of the multilayer structure used to solve the elastodynamic problem. The uppercase letter "M" denotes the sublayers that can be inserted between media I and II to mechanically couple these two media. The black (red) arrows represent the wave vectors of the longitudinal (transverse) polarized waves propagating in the $\pm x_1$-direction.

hypothesis is used ($\partial/\partial x_3 = 0$) because the layers and the laser line source are considered to be of infinite dimension in the $\mathbf{x}_3$-direction.

III. ELECTROMAGNETIC PROBLEM

In this section, the method for solving the electromagnetic problem in the multilayer structure, represented in Fig. 1, is detailed. Our work focuses on the simulation of laser-ultrasonic experiments performed in the thermoelastic regime. Thus, the aim is to obtain the power density Q of the energy dissipated into heat in the different media, following the approach of Born and Wolf.[20] The power density Q will then be used as the source term for the heat equation defined in Sec. IV.

A. Formulation of the electromagnetic problem

Under the assumptions presented in Sec. II, and using the Maxwell's equations, the electric vector $\mathbf{E}$ in the multilayer structure must satisfy the Helmholtz equation

$$\mathbf{V}^2\mathbf{E} + k^2\mathbf{E} = 0, \tag{1}$$

with the complex wavenumber

$$k = k' + \jmath k'', \quad k' = \Re\left(\frac{\omega_0}{c_0}n\right) \quad \text{and} \quad k'' = \Im\left(\frac{\omega_0}{c_0}n\right). \tag{2}$$

In Eq. (2), the constant c_0 is equal to the speed of light in vacuum, $\jmath$ is the unit imaginary number, the $\Re$ ($\Im$) symbol corresponds to the real (imaginary) part and n is the complex refractive index defined by the relation

$$n = n' + \jmath n'', \, n' = \Re(n) \text{ and } n'' = \Im(n). \tag{3}$$

In the literature, n'' is often called the extinction coefficient[21] or the attenuation index.[20] The complex refractive index n is also equal to

$$n = \sqrt{\mu\varepsilon_c} = \sqrt{\mu\left(\varepsilon + \jmath\frac{4\pi\sigma}{\omega_0}\right)}, \tag{4}$$

with ε_c the complex dielectric constant, ε the dielectric constant, μ the magnetic permeability, and σ the optical conductivity.

B. Propagation of the electromagnetic waves in the multilayer structure

In Fig. 1, a plane electromagnetic wave is incident on the medium I with an angle of incidence equal to θ_0. The incident electromagnetic wave is linearly polarized, and the electric vector $\mathbf{E}_0^+$ is in the plane $(\mathbf{x}_1, \mathbf{x}_2)$. This implies that the magnetic vector $\mathbf{H}_0^+$ is in the $\mathbf{x}_3$-direction [case of transverse magnetic (TM) waves]. Using Snell's laws, the electromagnetic waves that are reflected and transmitted in the different layers can be defined, as illustrated in Fig. 1. The analytic expressions of the electric vectors, in the different media at a point of vector position $\mathbf{x}$, are

$$\mathbf{E}_0 = \mathbf{E}_0^+ e^{-\jmath(\omega_0 t - \mathbf{k}_0^+ \cdot \mathbf{x})} + \mathbf{E}_0^- e^{-\jmath(\omega_0 t - \mathbf{k}_0^- \cdot \mathbf{x})}, \tag{5a}$$

$$\mathbf{E}_I = \mathbf{E}_I^+ e^{-\jmath(\omega_0 t - \mathbf{k}_I^+ \cdot \mathbf{x})} + \mathbf{E}_I^- e^{-\jmath(\omega_0 t - \mathbf{k}_I^- \cdot \mathbf{x})}, \tag{5b}$$

$$\mathbf{E}_{II} = \mathbf{E}_{II}^+ e^{-\jmath(\omega_0 t - \mathbf{k}_{II}^+ \cdot \mathbf{x})} + \mathbf{E}_{II}^- e^{-\jmath(\omega_0 t - \mathbf{k}_{II}^- \cdot \mathbf{x})}, \tag{5c}$$

$$\mathbf{E}_{III} = \mathbf{E}_{III}^+ e^{-\jmath(\omega_0 t - \mathbf{k}_{III}^+ \cdot \mathbf{x})}. \tag{5d}$$

The analytic expressions of the magnetic vectors are obtained using the relation

$$\mathbf{H} = \sqrt{\frac{\varepsilon_c}{\mu}}\mathbf{s} \times \mathbf{E}, \quad \text{with } \mathbf{s} = \frac{\mathbf{k}}{||\mathbf{k}||}. \tag{6}$$

Thus, the magnetic vectors in the different media, with $i = \{0, I, II\}$, are equal to

$$\mathbf{H}_i = -n_i/\mu_i(E_i^+ e^{\jmath\mathbf{k}_i^+ \cdot \mathbf{x}} + E_i^- e^{\jmath\mathbf{k}_i^- \cdot \mathbf{x}})e^{-\jmath\omega_0 t}\mathbf{x}_3, \tag{7a}$$

$$\mathbf{H}_{III} = -n_{III}/\mu_{III}E_{III}^+ e^{-\jmath(\omega_0 t - \mathbf{k}_{III}^+ \cdot \mathbf{x})}\mathbf{x}_3. \tag{7b}$$

To determine the amplitudes E_0^-, E_I^+, E_I^-, E_{II}^+, E_{II}^-, and E_{III}^+, six boundary conditions are applied, ensuring the continuity of the projected electric field along the $\mathbf{x}_2$-axis and the projected magnetic field along the $\mathbf{x}_3$-axis at each interfaces between the different media. At $x_1 = 0$ and $x_1 = H$, these boundary conditions lead to the writing of Eqs. (8a), (8b), (8d), and (8e). Between media I and II, the boundary conditions are expressed in Eq. (8c), using the transfer matrix method (pp. 26–60 in Ref. 22). This transfer matrix $[L^{EM}]$ takes into account the propagation of electromagnetic waves in the sublayers located between media I and II.[23]

$$\mathbf{E}_0|_{x_1=0} \cdot \mathbf{x}_2 = \mathbf{E}_I|_{x_1=0} \cdot \mathbf{x}_2, \tag{8a}$$

$$\mathbf{H}_0|_{x_1=0} \cdot \mathbf{x}_3 = \mathbf{H}_I|_{x_1=0} \cdot \mathbf{x}_3, \tag{8b}$$

$$\begin{bmatrix} \mathbf{E}_{\mathrm{I}} \cdot \mathbf{x}_2 \\ \mathbf{H}_{\mathrm{I}} \cdot \mathbf{x}_3 \end{bmatrix}_{x_1=h_1} = \begin{bmatrix} L^{EM} \end{bmatrix}_{2\times2} \begin{bmatrix} \mathbf{E}_{\mathrm{II}} \cdot \mathbf{x}_2 \\ \mathbf{H}_{\mathrm{II}} \cdot \mathbf{x}_3 \end{bmatrix}_{x_1=h_1+\Delta h}, \quad (8c)$$

$$\mathbf{E}_{\mathrm{II}}|_{x_1=H} \cdot \mathbf{x}_2 = \mathbf{E}_{\mathrm{III}}|_{x_1=H} \cdot \mathbf{x}_2, \quad (8d)$$

$$\mathbf{H}_{\mathrm{II}}|_{x_1=H} \cdot \mathbf{x}_3 = \mathbf{H}_{\mathrm{III}}|_{x_1=H} \cdot \mathbf{x}_3. \quad (8e)$$

Using the Eqs. (5a)–(5d) and Eqs. (7a), (7b) in the calculation of the boundary conditions [Eqs. (8a)–8e)], it follows that the linear system to solve to determine the ratio of the amplitudes of the reflected/transmitted electromagnetic waves to the amplitude of the incident electromagnetic wave is

$$\begin{bmatrix} A_{11}^E & A_{12}^E & A_{13}^E & 0 & 0 & 0 \\ A_{21}^E & A_{22}^E & A_{23}^E & 0 & 0 & 0 \\ 0 & A_{32}^E & A_{33}^E & A_{34}^E & A_{35}^E & 0 \\ 0 & A_{42}^E & A_{43}^E & A_{44}^E & A_{45}^E & 0 \\ 0 & 0 & 0 & A_{54}^E & A_{55}^E & A_{56}^E \\ 0 & 0 & 0 & A_{64}^E & A_{65}^E & A_{66}^E \end{bmatrix} \begin{bmatrix} R_0^- \\ R_{\mathrm{I}}^+ \\ R_{\mathrm{I}}^- \\ R_{\mathrm{II}}^+ \\ R_{\mathrm{II}}^- \\ R_{\mathrm{III}}^+ \end{bmatrix} = \begin{bmatrix} \cos\theta_0 \\ -n_0/\mu_0 \\ 0 \\ 0 \\ 0 \\ 0 \end{bmatrix}. \quad (9)$$

To obtain a well-conditioned matrix (see the supplementary material[23] for detailed expressions of the coefficients A_{ij}^E), the unknowns of Eq. (9) are written as

$$R_0^- = \frac{E_0^-}{E_0^+}, \quad R_{\mathrm{I}}^+ = \frac{E_{\mathrm{I}}^+}{E_0^+}, \quad R_{\mathrm{I}}^- = \frac{E_{\mathrm{I}}^-}{E_0^+} e^{\beta_{\mathrm{I}}(\theta_1)h_1/2},$$

$$R_{\mathrm{II}}^+ = \frac{E_{\mathrm{II}}^+}{E_0^+} e^{-\beta_{\mathrm{II}}(\theta_2)(h_1+\Delta h/2)}, \quad R_{\mathrm{II}}^- = \frac{E_{\mathrm{II}}^-}{E_0^+} e^{\beta_{\mathrm{II}}(\theta_2)H/2},$$

$$R_{\mathrm{III}}^+ = \frac{E_{\mathrm{III}}^+}{E_0^+}, \quad (10)$$

with the inverse expressions of the optical penetrations which are equal to[24]

$$\beta_{\mathrm{I}}(\theta_1) = 2\left[k_{\mathrm{I}}'\Im(\cos\theta_1) + k_{\mathrm{I}}''\Re(\cos\theta_1)\right], \quad (11a)$$

$$\beta_{\mathrm{II}}(\theta_2) = 2\left[k_{\mathrm{II}}'\Im(\cos\theta_2) + k_{\mathrm{II}}''\Re(\cos\theta_2)\right]. \quad (11b)$$

The amplitudes of the electromagnetic waves are now determined and will be used to obtain the power density Q of the energy dissipated into heat in the media.

C. Determination of the power density Q

The power density Q is obtained by applying the Poynting theorem and by assuming that the convection current density $\mathbf{j}_v$ is equal to zero (see the hypothesis formulated in Sec. II). Therefore,

$$Q = -\mathbf{\nabla} \cdot \langle \mathbf{S} \rangle, \quad (12)$$

with the time average of the Poynting vector

$$\langle \mathbf{S} \rangle = \frac{c_0}{8\pi} \Re(\mathbf{E} \times \bar{\mathbf{H}}). \quad (13)$$

In Eq. (13), $\bar{\mathbf{H}}$ is the conjugate of the magnetic vector $\mathbf{H}$. Finally, using the Eqs. (5a)–(5d) and Eqs. (7a), (7b), the expressions of the power density Q in media I and II are

$$Q_{\mathrm{I}}(x_1) = I_0 \Lambda_{\mathrm{I}}(\theta_1)\left[|R_{\mathrm{I}}^+|^2 e^{-\beta_{\mathrm{I}}(\theta_1)x_1} + |R_{\mathrm{I}}^-|^2 e^{\beta_{\mathrm{I}}(\theta_1)(x_1-h_1)}\right], \quad (14a)$$

$$\begin{aligned} Q_{\mathrm{II}}(x_1) = I_0 \Lambda_{\mathrm{II}}(\theta_2)&\left[|R_{\mathrm{II}}^+|^2 e^{-\beta_{\mathrm{II}}(\theta_2)[x_1-(h_1+\Delta h)]} \right. \\ &\left. + |R_{\mathrm{II}}^-|^2 e^{\beta_{\mathrm{II}}(\theta_2)(x_1-H)}\right], \end{aligned} \quad (14b)$$

with $I_0 = c_0|E_0^+|^2/(8\pi)$ the intensity of the incident electromagnetic wave and

$$\Lambda_{\mathrm{I}}(\theta_1) = \beta_{\mathrm{I}}(\theta_1)\Re(\bar{n}_{\mathrm{I}}\cos\theta_1)/\mu_{\mathrm{I}}, \quad (15a)$$

$$\Lambda_{\mathrm{II}}(\theta_2) = \beta_{\mathrm{II}}(\theta_2)\Re(\bar{n}_{\mathrm{II}}\cos\theta_2)/\mu_{\mathrm{II}}, \quad (15b)$$

which, multiplied by the squared modulus of the ratio R_i^+ (R_i^-), stands for the intensity transmission (reflection) of an electromagnetic plane wave under oblique incidence. The power densities $Q_{\mathrm{I}}(x_1)$ and $Q_{\mathrm{II}}(x_1)$ will be used in Sec. IV as the source terms for the heat equation. Note that in Sec. IV, the power density Q will depend on x_1 and also on x_2 to consider the lateral distribution of intensity of the incident laser line source.[24]

IV. HEAT DIFFUSION PROBLEM

The aim of this section is to determine the temperature fields in media I and II by considering heat conduction. Therefore, the heat equation to be solved is

$$\mathbf{\nabla} \cdot (\underline{\lambda}\mathbf{\nabla}T) + Q(x_1, x_2, t) = \rho c_p \frac{\partial T}{\partial t}, \quad (16)$$

with $\underline{\lambda}$ the second-order tensor of thermal conductivity, T the temperature field, Q the power density defined in Sec. III, ρ the density, and c_p the specific heat. As mentioned above, the power density Q depends here on x_1 and x_2 to consider the lateral distribution of intensity of the incident laser line source.[24] Assuming that the media are homogeneous, the tensor of thermal conductivity in Eq. (16) is taken out of the divergence operator to obtain

$$\underline{\lambda}\mathbf{\nabla}^2 T + Q(x_1, x_2, t) = \rho c_p \frac{\partial T}{\partial t}. \quad (17)$$

In addition, each layer is assumed to be orthotropic, with $\mathbf{x}_1$ and $\mathbf{x}_2$ as principal axes, so the thermal conductivity tensor is written as a diagonal matrix

$$\underline{\lambda} = \begin{bmatrix} \lambda_{11} & 0 \\ 0 & \lambda_{22} \end{bmatrix}. \quad (18)$$

The heat equation will be solved in the Fourier domain by considering harmonic solutions. Therefore, Eq. (17) gives

2068   J. Acoust. Soc. Am. **150** (3), September 2021

Hodé *et al.*

$$D_{11}\frac{\partial^2 \hat{T}}{\partial x_1^2} - (\jmath\omega + D_{22}k_2^2)\hat{T} = -\frac{1}{\rho c_p}\hat{Q}(x_1, k_2, \omega), \quad (19)$$

with thermal diffusivities $D_{11} = (\lambda_{11}/\rho c_p)$ and $D_{22} = (\lambda_{22}/\rho c_p)$. The convention chosen for the double Fourier transform in space x_2 and time t (denoted by the hat "^") is given by

$$\hat{T}(x_1, k_2, \omega) = \frac{1}{2\pi}\iint_{-\infty}^{+\infty} T(x_1, x_2, t)e^{-\jmath(\omega t - k_2 x_2)}\, dt\, dx_2.$$
$$(20)$$

The source term $\hat{Q}(x_1, k_2, \omega)$, expressed in the Fourier domain in Eq. (19), is equal to

$$\hat{Q}(x_1, k_2, \omega) = Q(x_1)\, F(\omega)\, G(x_1, k_2), \quad (21)$$

with $Q(x_1)$ the power density determined in Sec. III. $F(\omega)$ and $G(x_1, k_2)$ are the Fourier transforms of the pulse distributions in time and space, $f(t)$ and $g(x_1, x_2)$, respectively. Their expressions are here considered to be

$$F(\omega) = \frac{1}{\sqrt{2\pi}}\int_{-\infty}^{+\infty} f(t)e^{-\jmath\omega t}\, dt$$
$$= \frac{1}{\sqrt{2\pi}}e^{-\tau_p^2\omega^2/(16\ln 2)}, \quad (22a)$$

$$G(x_1, k_2) = \frac{1}{\sqrt{2\pi}}\int_{-\infty}^{+\infty} g(x_1, x_2)e^{\jmath k_2 x_2}\, dx_2$$
$$= \frac{1}{\sqrt{2\pi}\cos\theta}e^{-a_s^2 k_2^2/(16\ln 2\cos^2\theta)}e^{\jmath k_2 x_1 \tan\theta}, \quad (22b)$$

with τ_p the pulse duration at half maximum [full width at half-maximum (FWHM)] of the Gaussian function $f(t)$ and a_s the source width at half maximum (FWHM) of the tilted Gaussian beam mathematically represented by $g(x_1, x_2)$.[24] Note that, in Eq. (22b), the angle θ refers to the angle between the $\mathbf{x}_1$-direction and the direction of refraction in the medium in which the heat diffusion problem is solved. Homogeneous and particular solutions are searched to solve Eq. (19) in media I and II and are detailed in Sec. IV A and in Sec. IV B, respectively.

A. Homogeneous solutions of the heat equation

In each layer $i = \{I, II\}$, homogeneous solutions $\hat{T}_h^i$ of the heat equation, expressed without the source term $-(1/\rho c_p)\hat{Q}^i(x_1, k_2, \omega)$ in Eq. (19), are sought in the form

$$\hat{T}_h^i(x_1, k_2, \omega) = \hat{T}_h^{i\pm}(k_2, \omega)e^{\pm\Gamma_1^i x_1}. \quad (23)$$

By injecting Eq. (23) into the homogeneous heat equation, we obtain

$$\left[D_{11}^i\Gamma_1^{i\,2} - (\jmath\omega + D_{22}^i k_2^2)\right]\hat{T}_h^{i\pm}(k_2, \omega)e^{\pm\Gamma_1^i x_1} = 0, \quad (24)$$

which results in

$$\Gamma_1^i = \sqrt{\frac{\jmath\omega + D_{22}^i k_2^2}{D_{11}^i}}. \quad (25)$$

Therefore, the homogeneous solutions are the sum of two thermal waves that propagate in the $\pm x_1$-direction, as illustrated in Fig. 2 and given by

$$\hat{T}_h^i(x_1, k_2, \omega) = \hat{T}_h^{i+}(k_2, \omega)e^{-\Gamma_1^i x_1} + \hat{T}_h^{i-}(k_2, \omega)e^{\Gamma_1^i x_1}, \quad (26)$$

with the coefficients $\hat{T}_h^{i+}(k_2, \omega)$ and $\hat{T}_h^{i-}(k_2, \omega)$ to be determined later using the boundary conditions.

B. Particular solutions of the heat equation

Particular solutions $\hat{T}_p^i$ are searched in the form of the source terms specified in Eqs. (14a), (14b) for media I and II, which gives

$$\hat{T}_p^I(x_1, k_2, \omega) = \hat{T}_p^{I+}(k_2, \omega)e^{-\beta_I(\theta_1)x_1}e^{\jmath k_2 \tan\theta_1 x_1}$$
$$+ \hat{T}_p^{I-}(k_2, \omega)e^{\beta_I(\theta_1)(x_1-h_1)}e^{-\jmath k_2 \tan\theta_1 x_1}, \quad (27a)$$

$$\hat{T}_p^{II}(x_1, k_2, \omega) = \hat{T}_p^{II+}(k_2, \omega)e^{-\beta_{II}(\theta_2)[x_1-(h_1+\Delta h)]}e^{\jmath k_2 \tan\theta_2 x_1}$$
$$+ \hat{T}_p^{II-}(k_2, \omega)e^{\beta_{II}(\theta_2)(x_1-H)}e^{-\jmath k_2 \tan\theta_2 x_1}. \quad (27b)$$

Then, Eqs. (27a), (27b) are fed into the heat equation (19) to obtain the four coefficients

$$\hat{T}_p^{i+} = -\frac{\hat{Q}_i^+}{\rho^i c_p^i}\left[D_{11}^i d_i^2 - (\jmath\omega + D_{22}^i k_2^2)\right]^{-1}, \quad (28a)$$

$$\hat{T}_p^{i-} = -\frac{\hat{Q}_i^-}{\rho^i c_p^i}\left[D_{11}^i d_i^2 - (\jmath\omega + D_{22}^i k_2^2)\right]^{-1}, \quad (28b)$$

with $d_i = \beta_i - \jmath k_2 \tan\theta_i$ and the power densities Q_i^+ and Q_i^- expressed as a function of the parameters I_0, $\Lambda_i(\theta_i)$ and $|R_i^\pm|$ given in Sec. III:

$$\hat{Q}_i^+ = I_0\, \Lambda_i(\theta_i)\, |R_i^+|^2\, F(\omega)\, G(k_2), \quad (29a)$$

$$\hat{Q}_i^- = I_0\, \Lambda_i(\theta_i)\, |R_i^-|^2\, F(\omega)\, G(k_2). \quad (29b)$$

C. Application of the boundary conditions

As mentioned in Sec. IV A, the boundary conditions are applied to determine the four coefficients $\hat{T}_h^{i+}(k_2, \omega)$ and $\hat{T}_h^{i-}(k_2, \omega)$ of the homogeneous solutions. At $x_1 = 0$ and $x_1 = H$, the heat fluxes are conserved, and the thermal convection is taken into account with the heat transfer coefficient h_c. Hence, using the Fourier's law and the Newton's law,[25] it gives

$$\lambda_{11}^I\frac{\partial \hat{T}_I}{\partial x_1}\Big|_{x_1=0} = h_c\left(\hat{T}_I|_{x_1=0} - \hat{T}_\infty\right), \quad (30)$$

$$\lambda_{11}^{II}\frac{\partial \hat{T}_{II}}{\partial x_1}\Big|_{x_1=H} = -h_c\left(\hat{T}_{II}|_{x_1=H} - \hat{T}_\infty\right), \quad (31)$$

with $\hat{T}_\infty$ the double Fourier transform of the temperature when x_1 approaches infinity. Furthermore, if heat diffusion

J. Acoust. Soc. Am. **150** (3), September 2021

Hodé *et al.*   2069

losses are neglected in the $\mathbf{x}_2$-direction for each i-th sublayer and $\Gamma_1^i h_i \ll 1$ is assumed, i.e., thermally thin sublayer, with Γ_1^i defined in Eq. (25) and h_i the thickness of the i-th sublayer, the heat flux is conserved between media I and II, resulting in

$$\lambda_{11}^I \frac{\partial \hat{T}_I}{\partial x_1}\bigg|_{x_1=h_1} = \lambda_{11}^{II} \frac{\partial \hat{T}_{II}}{\partial x_1}\bigg|_{x_1=(h_1+\Delta h)}. \tag{32}$$

However, the temperature field may be discontinuous, which results in

$$\lambda_{11}^I \frac{\partial \hat{T}_I}{\partial x_1}\bigg|_{x_1=h_1} = \frac{\hat{T}_{II}|_{x_1=(h_1+\Delta h)} - \hat{T}_I|_{x_1=h_1}}{R_c}, \tag{33}$$

with R_c the thermal resistance defined as

$$R_c = \sum_{i=1}^{N_{\text{sublayers}}} \frac{h_i}{\lambda_{11}^i}, \tag{34}$$

with $N_{\text{sublayers}}$ the total number of sublayers between media I and II and λ_{11}^i the thermal conductivity of each sublayer. By replacing the temperature field in the boundary conditions [Eqs. (30)–(33)] by the sum of the homogeneous and particular solutions given in Eqs. (26), (27a), (27b), we obtain the following linear system:

$$\begin{bmatrix} A_{11}^T & A_{12}^T & 0 & 0 \\ A_{21}^T & A_{22}^T & A_{23}^T & A_{24}^T \\ A_{31}^T & A_{32}^T & A_{33}^T & A_{34}^T \\ 0 & 0 & A_{43}^T & A_{44}^T \end{bmatrix} \begin{bmatrix} \hat{T}_h^{I+} \\ {}^\star\hat{T}_h^{I-} \\ {}^\star\hat{T}_h^{II+} \\ {}^\star\hat{T}_h^{II-} \end{bmatrix} = \begin{bmatrix} B_1^T \\ B_2^T \\ B_3^T \\ B_4^T \end{bmatrix}. \tag{35}$$

To obtain a well-conditioned matrix,[23] the unknowns of Eq. (35), with the symbol "*", are written as[13]

$$\begin{aligned} {}^\star\hat{T}_h^{I-} &= \hat{T}_h^{I-} e^{\Gamma_1^I h_1}, \quad {}^\star\hat{T}_h^{II+} = \hat{T}_h^{II+} e^{-\Gamma_1^{II}(h_1+\Delta h)}, \\ {}^\star\hat{T}_h^{II-} &= \hat{T}_h^{II-} e^{\Gamma_1^{II} H}. \end{aligned} \tag{36}$$

Finally, the temperature fields $\hat{T}^I(x_1, k_2, \omega)$ and $\hat{T}^{II}(x_1, k_2, \omega)$ are fully determined by the expressions

$$\begin{aligned} \hat{T}^I(x_1, k_2, \omega) &= \hat{T}_h^{I+}(k_2, \omega) e^{-\Gamma_1^I x_1} \\ &\quad + {}^\star\hat{T}_h^{I-}(k_2, \omega) e^{\Gamma_1^I(x_1-h_1)} + \hat{T}_p^I(x_1, k_2, \omega), \end{aligned} \tag{37a}$$

$$\begin{aligned} \hat{T}^{II}(x_1, k_2, \omega) &= {}^\star\hat{T}_h^{II+}(k_2, \omega) e^{-\Gamma_1^{II}[x_1-(h_1+\Delta h)]} \\ &\quad + {}^\star\hat{T}_h^{II-}(k_2, \omega) e^{\Gamma_1^{II}(x_1-H)} + \hat{T}_p^{II}(x_1, k_2, \omega). \end{aligned} \tag{37b}$$

V. ELASTODYNAMIC PROBLEM

The absorption of electromagnetic waves by the layers, as well as the thermal diffusion, have been detailed in

Secs. III and IV, respectively. These two physical phenomena are at the origin of the elastic wave generation that occurs in the multilayer represented in Fig. 3. The elastodynamic problem is addressed in this section. Under the assumptions presented in Sec. II and the small perturbation hypothesis, the equation of motion is

$$\rho \frac{\partial^2 \mathbf{u}}{\partial t^2}(x_1, x_2, t) = \nabla \cdot \underline{\sigma}(x_1, x_2, t), \tag{38}$$

with ρ the density, $\mathbf{u}$ the displacement vector and $\underline{\sigma}$ the Cauchy stress tensor. Using Hooke's law, the stress tensor is equal to

$$\underline{\sigma}(x_1, x_2, t) = \underline{\underline{C}} : \underline{\varepsilon}(x_1, x_2, t) - \underline{\underline{C}} : \underline{\alpha}\Delta T(x_1, x_2, t), \tag{39}$$

with $\underline{\underline{C}}$ the fourth-order stiffness tensor, ":" the double dot product, $\underline{\varepsilon}$ the second-order strain tensor, $\underline{\alpha}$ the second-order thermal expansion tensor, and ΔT the elevation of temperature in the medium. Media I and II are assumed to be orthotropic with $\mathbf{x}_1$ and $\mathbf{x}_2$ as principal axes. In Voigt notation, Eq. (39) gives

$$\begin{bmatrix} \sigma_{11} \\ \sigma_{22} \\ \sigma_{12} \end{bmatrix} = \begin{bmatrix} C_{11} & C_{12} & 0 \\ C_{12} & C_{22} & 0 \\ 0 & 0 & C_{66} \end{bmatrix} \left(\begin{bmatrix} \varepsilon_{11} \\ \varepsilon_{22} \\ 2\varepsilon_{12} \end{bmatrix} - \begin{bmatrix} \alpha_{11} \\ \alpha_{22} \\ 0 \end{bmatrix} \Delta T \right), \tag{40}$$

with $\varepsilon_{ij} = \frac{1}{2}\left(\partial u_i/\partial x_j + \partial u_j/\partial x_i\right)$. Viscoelastic attenuation can be introduced by considering complex elastic coefficients with the imaginary part related to the attenuation. For the Kelvin-Voigt model

$$\underline{\underline{C}}^* = \underline{\underline{C}} + \jmath\omega\underline{\underline{\eta}}, \tag{41}$$

with $\underline{\underline{\eta}}$ the fourth-order viscosity tensor. To lighten the notations, the elastic coefficients are written without the symbol "*" in the following. The use of Eq. (39) in Eq. (38) and the projection of Eq. (38) onto $\mathbf{x}_1$-axis and $\mathbf{x}_2$-axis yield the following elastodynamic equations in the Fourier domain:

$$\begin{aligned} C_{11}\frac{\partial^2 \hat{u}_1}{\partial x_1^2} &- \jmath k_2(C_{12}+C_{66})\frac{\partial \hat{u}_2}{\partial x_1} \\ &+ \left(\rho\omega^2 - C_{66}k_2^2\right)\hat{u}_1 = C_{\alpha_1}\frac{\partial \hat{T}}{\partial x_1}, \end{aligned} \tag{42a}$$

$$\begin{aligned} C_{66}\frac{\partial^2 \hat{u}_2}{\partial x_1^2} &- \jmath k_2(C_{12}+C_{66})\frac{\partial \hat{u}_1}{\partial x_1} \\ &+ \left(\rho\omega^2 - C_{22}k_2^2\right)\hat{u}_2 = -\jmath k_2 C_{\alpha_2}\hat{T}, \end{aligned} \tag{42b}$$

with $C_{\alpha_1} = C_{11}\alpha_{11} + C_{12}\alpha_{22}$, $C_{\alpha_2} = C_{12}\alpha_{11} + C_{22}\alpha_{22}$. In this section, the convention for the double Fourier transform, in space x_2 and time t, is the same as the one given in Eq. (20). The solution of Eqs. (42a), (42b) is the sum of the homogeneous solution $\hat{\mathbf{u}}_h(x_1, k_2, \omega)$ and the particular solution $\hat{\mathbf{u}}_p(x_1, k_2, \omega)$ as detailed in Sec. V A and Sec. V B.

A. Homogeneous solutions of the elastodynamic equations

The solutions of the homogeneous elastodynamic equations, Eqs. (42a), (42b) without the source terms $C_{\alpha_1}\partial\hat{T}/\partial x_1$ and $-\jmath k_2 C_{\alpha_2}\hat{T}$, are sought in the form of

$$\hat{\mathbf{u}}_h(x_1, k_2, \omega) = \hat{\mathbf{U}}_h(k_2, \omega)e^{-\jmath k_1 x_1}. \tag{43}$$

By injecting Eq. (43) in the homogeneous elastodynamic Eqs. (42a), (42b), we obtain

$$\begin{bmatrix} a_{11} - k_1^2 C_{11} & -k_1 a_{12} \\ -k_1 a_{12} & a_{22} - k_1^2 C_{66} \end{bmatrix}\begin{bmatrix} \hat{U}_{1h} \\ \hat{U}_{2h} \end{bmatrix} = \begin{bmatrix} 0 \\ 0 \end{bmatrix}, \tag{44}$$

with $a_{11} = \rho\omega^2 - k_2^2 C_{66}$, $a_{22} = \rho\omega^2 - k_2^2 C_{22}$, and $a_{12} = k_2(C_{12} + C_{66})$. Then, by imposing that the determinant of the 2×2 matrix of Eq. (44) is zero, we get the quadratic equation

$$aX^2 + bX + c = 0, \tag{45}$$

with $X = k_1^2$ and the coefficients of the quadratic equation: $a = C_{11}C_{66}$, $b = -(C_{11}a_{22} + C_{66}a_{11} + a_{12}^2)$, $c = a_{11}a_{22}$. The two solutions of Eq. (45) are

$$X_{\pm} = \frac{-b\pm\sqrt{b^2 - 4ac}}{2a}, \tag{46a}$$

which gives four eigenvalues for the wavenumber k_1. Thus, the homogeneous solution is the linear combination of two longitudinal (L) and two transverse (T) polarized waves, which are traveling along the positive and negative directions of the $\mathbf{x}_1$-axis as illustrated in Fig. 3 and defined by the equation

$$\hat{\mathbf{u}}_h(x_1, k_2, \omega) = \sum_{n=\{L,T\}} A^{n+}\hat{\mathbf{U}}_h^{n+}(k_2, \omega)e^{-\jmath k_1^n x_1}$$
$$+ A^{n-}\hat{\mathbf{U}}_h^{n-}(k_2, \omega)e^{\jmath k_1^n x_1}. \tag{47}$$

In Eq. (47), $k_1^L = \sqrt{X_-}$ and $k_1^T = \sqrt{X_+}$ are the projections of the longitudinal and transverse wave vectors along the $\mathbf{x}_1$-axis, respectively. In addition, $A^{n\pm}$ refer to the wave amplitudes that are subsequently determined by applying the boundary conditions, and $\hat{\mathbf{U}}_h^{n\pm}$ are the eigenvectors that are equal to

$$\hat{\mathbf{U}}_h^{n\pm}(k_2, \omega) = \begin{bmatrix} \hat{U}_{1h}^{n\pm} \\ \hat{U}_{2h}^{n\pm} \end{bmatrix} = \begin{bmatrix} a_{22} - (k_1^n)^2 C_{66} \\ \pm k_1^n a_{12} \end{bmatrix}. \tag{48a}$$

B. Particular solutions of the elastodynamic equations

The particular solutions are searched following the form of the source terms $C_{\alpha_1}\partial\hat{T}/\partial x_1$ and $-\jmath k_2 C_{\alpha_2}\hat{T}$ of Eqs. (42a), (42b). Therefore, using the analytic expression of the

temperature fields $\hat{T}$ in media I and II, given in Eqs. (37a), (37b), the particular solutions are

$$\hat{\mathbf{u}}_p^I = \hat{\mathbf{U}}_{p\Gamma}^{I+}e^{-\Gamma_1^I x_1} + \hat{\mathbf{U}}_{p\Gamma}^{I-}e^{\Gamma_1^I(x_1 - h_1)}$$
$$+ \hat{\mathbf{U}}_{p\beta}^{I+}e^{-\beta_1(\theta_1)x_1}e^{\jmath k_2 \tan\theta_1 x_1}$$
$$+ \hat{\mathbf{U}}_{p\beta}^{I-}e^{\beta_1(\theta_1)(x_1 - h_1)}e^{-\jmath k_2 \tan\theta_1 x_1}, \tag{49a}$$

$$\hat{\mathbf{u}}_p^{II} = \hat{\mathbf{U}}_{p\Gamma}^{II+}e^{-\Gamma_1^{II}[x_1 - (h_1 + \Delta h)]} + \hat{\mathbf{U}}_{p\Gamma}^{II-}e^{\Gamma_1^{II}(x_1 - H)}$$
$$+ \hat{\mathbf{U}}_{p\beta}^{II+}e^{-\beta_{II}(\theta_2)[x_1 - (h_1 + \Delta h)]}e^{\jmath k_2 \tan\theta_2 x_1}$$
$$+ \hat{\mathbf{U}}_{p\beta}^{II-}e^{\beta_{II}(\theta_2)(x_1 - H)}e^{-\jmath k_2 \tan\theta_2 x_1}. \tag{49b}$$

To obtain the four vectors $\hat{\mathbf{U}}_{p\beta}^{I+}$, $\hat{\mathbf{U}}_{p\beta}^{I-}$, $\hat{\mathbf{U}}_{p\beta}^{II+}$ and $\hat{\mathbf{U}}_{p\beta}^{II-}$, which are related to the optical penetration of the electromagnetic waves in media I and II, each term of Eqs. (49a), (49b) is injected into the elastodynamic Eqs. (42a), (42b). Thus, four linear systems with the form

$$\begin{bmatrix} a_{11}^i + C_{11}^i d_i^2 & \pm\jmath a_{12}^i d_i \\ \pm\jmath a_{12}^i d_i & a_{22}^i + C_{66}^i d_i^2 \end{bmatrix}\begin{bmatrix} \hat{U}_{1p\beta}^{i\pm} \\ \hat{U}_{2p\beta}^{i\pm} \end{bmatrix} = \begin{bmatrix} -C_{\alpha_1}^i d_i(\pm\hat{T}_p^{i\pm}) \\ -\jmath k_2 C_{\alpha_2}^i \hat{T}_p^{i\pm} \end{bmatrix}, \tag{50}$$

have to be solved, with $i = \{I, II\}$ and $d_i = \beta_i - \jmath k_2 \tan\theta_i$. The same procedure is applied to calculate the four vectors $\hat{\mathbf{U}}_{p\Gamma}^{I+}$, $\hat{\mathbf{U}}_{p\Gamma}^{I-}$, $\hat{\mathbf{U}}_{p\Gamma}^{II+}$, and $\hat{\mathbf{U}}_{p\Gamma}^{II-}$ of Eqs. (49a), 49b), which are linked to the thermal diffusion in media I and II. Four other linear systems have to be solved.

C. Application of the boundary conditions

The homogeneous and particular solutions of the elastodynamic Eqs. (42a), (42b) have been determined in Sec. V A and Sec. V B. Consequently, the last step is to apply the boundary conditions to find the eight amplitudes $A_i^{n\pm}$, with $n = \{L, T\}$ and $i = \{I, II\}$, of the eight elastic waves that propagate in media I and II. In Fig. 3, the upper surface of medium I (at $x_1 = 0$) and the lower surface of medium II (at $x_1 = H$) are considered as free surfaces. Thus, four boundary conditions are given by

$$\hat{\sigma}_{11}^I\big|_{x_1=0} = \hat{\sigma}_{12}^I\big|_{x_1=0} = 0, \tag{51}$$

$$\hat{\sigma}_{11}^{II}\big|_{x_1=H} = \hat{\sigma}_{12}^{II}\big|_{x_1=H} = 0. \tag{52}$$

Using the mechanical coupling between media I and II, four other boundary conditions are

$$\begin{bmatrix} \hat{u}_1^I \\ \hat{u}_2^I \\ \hat{\sigma}_{11}^I \\ \hat{\sigma}_{12}^I \end{bmatrix}_{x_1=h_1} = \big[L^M\big]_{4\times4}\begin{bmatrix} \hat{u}_1^{II} \\ \hat{u}_2^{II} \\ \hat{\sigma}_{11}^{II} \\ \hat{\sigma}_{12}^{II} \end{bmatrix}_{x_1=h_1+\Delta h}, \tag{53}$$

with $[L^M]$ the transfer matrix (pp. 53–60 in Ref. 22) used to couple the displacements ($\hat{u}_1$, $\hat{u}_2$) and the stresses ($\hat{\sigma}_{11}$, $\hat{\sigma}_{12}$)

J. Acoust. Soc. Am. 150 (3), September 2021

Hodé et al. 2071

from medium I at $x_1 = h_1$, to medium II at $x_1 = h_1 + \Delta h$. The sublayers that can be inserted between media I and II will be taken into account through this transfer matrix. For instance, if we assume the continuity of displacements and stresses at the interface between media I and II (with $\Delta h = 0$), then $[L^M]$ is equal to the identity matrix.[23] Then, Eqs. (51)–(53) have to be solved to obtain the eight amplitudes of the elastic waves, taking care that the matrices are well conditioned [as it was done in Eqs. (35), (36)].[13] The complete solution in media I and II is equal to the linear combination of the homogeneous and particular solutions

$$\hat{\mathbf{u}}^i(x_1, k_2, \omega) = \hat{\mathbf{u}}_h^i(x_1, k_2, \omega) + \hat{\mathbf{u}}_p^i(x_1, k_2, \omega). \quad (54)$$

Finally, a double inverse Fourier transform in space x_2 and time t is performed to find the temporal solutions of the displacement field $u_i(x_1, x_2, t)$, with $i = \{1, 2\}$. Numerically, this double integration is carried out according to the approach proposed by Bouchon and Aid,[26] as well as Weaver et al.[27,28] The complex angular frequency $\omega^* = \omega - j\delta_\omega$ is used to slightly shift the analytic solutions in the imaginary plane to avoid the poles of the Rayleigh-Lamb waves. Then, the small positive constant δ_ω is removed after the double integration by multiplying the final result by $e^{\delta_\omega t}$:

$$u_i(x_1, x_2, t) = \frac{e^{\delta_\omega t}}{2\pi} \iint_{-\infty}^{+\infty} \hat{u}_i(x_1, k_2, \omega^*) e^{j(\omega t - k_2 x_2)} \, d\omega \, dk_2. \quad (55)$$

The semi-analytic method for solving electromagnetic, thermal, and elastodynamic problems was fully presented in Secs. III, IV, and V, respectively. The optical, thermal, and mechanical properties of materials are supposed independent of the temperature in the model, although this assumption could be too strong in some cases (materials with highly temperature-dependent properties, large laser fluence, …). Accounting for the temperature dependence of the physical properties in the model is not straightforward. It would require solving the equations numerically and not analytically, because the temperature field is time dependent, inducing all physical properties to be time dependent. However, this temperature dependence of the physical parameters can be neglected when the temperature increase in the material has a small effect. For instance, in an aluminum alloy (Al 2024), the change in velocity of acoustic waves is less than 1% below a temperature rise of 100 °C.[29] Thus, the temperature dependence may have an influence where the material temperature is locally higher than specified above (i.e., in the laser energy deposition area), but in the vast majority of the material, this assumption of temperature-independent physical parameters is justified. Examples of numerical results obtained with this simulation technique are presented below.

VI. NUMERICAL SIMULATION RESULTS

In this section, numerical results obtained with this semi-analytic model are reported. Some simulation parameters are unchanged for the three examples that are presented

later: the time range $t \in [0, 16.384]$ μs with the discretization step $\Delta t = 8.0 \, 10^{-3}$ μs; the position range $x_2 \in [-81.92, 81.92]$ mm with the discretization step $\Delta x_2 = 8.0 \, 10^{-2}$ mm. Hence, the maximum angular frequency ω is equal to $3.927 \, 10^2$ rad μs^{-1} (maximum frequency of 62.5 MHz) and the maximum wavenumber k_2 to $3.927 \, 10^1$ rad mm^{-1}. Note that the time step $\Delta t = 8.0 \, 10^{-3}$ μs is chosen according to the assumed bandwidth of an optical detection system (here, 0.7 MHz–40 MHz), mimicking actual conditions of experiments and which is taken into consideration in these simulations. Furthermore, the incident electromagnetic wave is defined by: the pulse duration $\tau_p = 8$ ns, the source width $a_s = 0.2$ mm, the intensity $I_0 = 0.2$ J mm^{-1}, the angle of incidence $\theta_0 = 0°$, and the electromagnetic wavelength $\lambda_{opt} = 532$ nm. Concerning the thermal parameters, the external temperature is set to $T_\infty = 293.15$ K, and the heat transfer coefficient is imposed to $h_c = 25$ W m^{-2} K^{-1}. The thermal resistance R_c is equal to zero in the following examples, although it can be easily modified with Eq. (34). Using these settings, three examples of the use of the developed semi-analytic model are described in Sec. VI A–VI C. The optical, thermal, and mechanical properties of the material used for the simulations are given in Table I.

A. Analysis of the guided elastic waves in an aluminum alloy plate

The first example is the frequency–wavenumber (f–k) diagrams depicting the normalized spectral density in dB,

$$\frac{|\hat{u}_1^I(x_1, k_2, \omega^*)|^2}{\max_{k_2, \omega^*} |\hat{u}_1^I(x_1, k_2, \omega^*)|^2}, \quad (56)$$

of a 1.23 mm-thick aluminum alloy plate for two different laser sources. In Fig. 4(a), the f–k diagram is obtained for a Gaussian laser pulse of duration $\tau_p = 8$ ns and source width $a_s = 0.2$ mm. The Fourier transforms of the pulse distribution in time and space are given by the expressions of $F(\omega)$ and $G(x_1, k_2)$ with $\theta_0 = 0°$ in Eqs. (22a) and (22b), respectively. Before applying the double inverse Fourier transform

TABLE I. Optical, thermal, and mechanical properties of the aluminum alloy (Al), SCHOTT N-BK7® glass and titanium (Ti).

	Al	N-BK7	Ti
n' (@ 532 nm)[30]	1.468	1.519	2.479
n'' (@ 532 nm)[30]	8.949	7.761 10^{-9}	3.351
μ	1.	1.	1.
λ_{11} (W m^{-1} K^{-1})	1.5 10^2	1.1	2.0 10^1
λ_{22} (W m^{-1} K^{-1})	1.5 10^2	1.1	2.0 10^1
c_p (J kg^{-1} K^{-1})	9.0 10^2	8.6 10^2	5.0 10^2
$\alpha_{11} = \alpha_{22}$ (K^{-1})	2.5 10^{-5}	8.3 10^{-6}	1.1 10^{-5}
C_{11} (GPa)	1.10 10^2	9.18 10^1	1.62 10^2
C_{12} (GPa)	5.69 10^1	2.38 10^1	6.90 10^1
C_{22} (GPa)	1.10 10^2	9.18 10^1	1.80 10^2
C_{66} (GPa)	2.65 10^1	3.40 10^1	4.67 10^1
ρ (kg m^{-3})	2.70 10^3	2.51 10^3	4.54 10^3

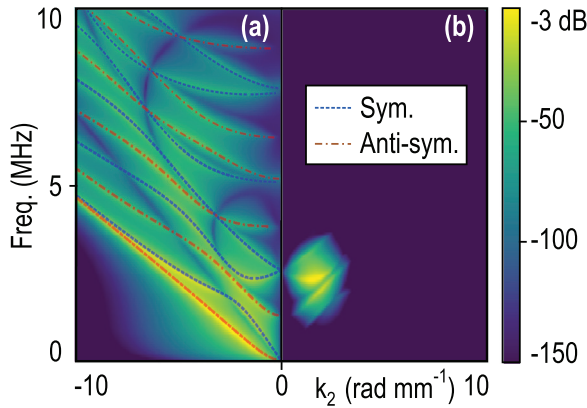2072   J. Acoust. Soc. Am. **150** (3), September 2021

Hodé et al.

FIG. 4. (Color online) Zoom views of f–k diagrams (plotted in dB with the colormap), for a 1.23 mm–thick aluminum alloy plate at $x_1 = 1.23$ mm, for two different laser sources. (a) Gaussian laser pulse ($\tau_p = 8$ ns, $a_s = 0.2$ mm). (b) Modulated laser source in time (tone burst of 2.5 MHz central frequency) and space (phase mask of 1.5 rad mm^{-1} central wavenumber). A good agreement is obtained with the dispersion curves simulated with the commercial software CIVA 2020 in dashed (dash-dotted) lines for symmetric (antisymmetric) modes, which are superimposed on the f–k diagrams calculated with the developed model.

introduced in Eq. (55), the displacement $\hat{u}_i(x_1, k_2, \omega^*)$ can indeed be used to analyze the dispersion of the waves guided along the $\mathbf{x}_2$-direction. In the case of a free plate, the modes shown in Fig. 4(a) correspond to the Lamb modes. Indeed, solving the problem in Fourier domains (time and space along the $\mathbf{x}_2$-direction) and with the 2D assumption is equivalent to look at the modal solutions of the free plate, propagating along the $\mathbf{x}_2$-direction, and where symmetric and antisymmetric modal decompositions are found along the $\mathbf{x}_1$-direction, which are the Lamb modes. Note that this f–k diagram contains, on top of the dispersive features of the modes, the information about their detectability with an interferometer sensitive only to the normal component of the displacement of the free surface. This Gaussian laser pulse allows excitement of a large number of Lamb modes because of the broadband content of $F(\omega)$ and $G(x_1, k_2)$. To excite specific modes only, the laser source can be modulated in time and space to select a particular area in the f–k diagram, as shown in Fig. 4(b). This can be easily implemented in the model by changing the expressions of $F(\omega)$ and $G(x_1, k_2)$ by the Fourier transform of the desired laser source modulated in time and space. To obtain the f–k diagram presented in Fig. 4(b), a tone burst of 2.5 MHz central frequency and a phase mask of 1.5 rad mm^{-1} central wavenumber k_2 were used.

The calculation time to obtain $\hat{u}_i(x_1, k_2, \omega^*)$, at a given x_1 position and for all the values of ω^* and k_2 vectors, is equal to 1 min 37 s $\pm$ 6 s (with an Intel® Core™ i7-6500U CPU @ 2.5 GHz, 16.0 GB RAM). The time domain signals as a function of x_2 can be obtained by applying the double inverse Fourier transform of $\hat{u}_i(x_1, k_2, \omega^*)$, which only adds 0.2 s to the previous calculation time.

Among other useful applications, the possibility, offered by the semi-analytic model proposed here, to analyze the influence of $F(\omega)$ and $G(x_1, k_2)$ on simulated f–k
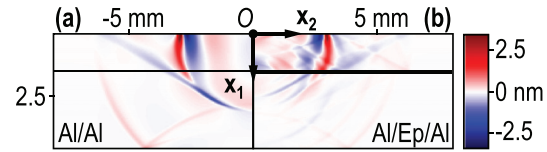

FIG. 5. (Color online) Normal displacements $u_1(x_1, x_2, t)$ simulated at $t = 1\,\mu$s in (a) a bilayer Al (1.5 mm)/Al (3.1 mm) and (b) a trilayer Al (1.5 mm)/Epoxy (0.1 mm)/Al (3.0 mm). See the supplementary material (Ref. 23) for the animations.

diagrams is of interest to help design the temporal and spatial profiles of the laser source to excite and detect specific Lamb modes. This type of analysis can be performed on more complex structures such as those presented below.

B. Bilayer/trilayer with interfacial stiffnesses

The second example deals with a bilayer composed of two aluminum alloy (Al) plates of 1.5 and 3.1 mm [Fig. 5(a)] and a trilayer Al (1.5 mm)/Epoxy (0.1 mm)/Al (3.0 mm) [Fig. 5(b)]. The normal displacement $u_1(x_1, x_2, t)$, generated by a Gaussian laser pulse of duration $\tau_p = 8$ ns and source width $a_s = 0.2$ mm, is obtained by solving numerically Eq. (55) for $x_1 \in [0, 4.6\,\text{mm}]$, with the positive constant $\delta_\omega = 0.4$ rad μs^{-1}. The snapshot of the normal displacement at $t = 1\,\mu$s is represented in Fig. 5. The heat source is located at the origin of the Cartesian coordinate system because the optical penetration depth in aluminum is equal to $1/\beta = 4.7$ nm (@ $\theta_0 = 0°$ and $\lambda_{\text{opt}} = 532$ nm).

In Fig. 5(a), two distributions of normal and transverse interfacial stiffnesses, equal to $K_N = K_T = \infty$ kN mm^{-3}, are inserted between the two Al plates. Thus, a perfect continuity of displacements and stresses is imposed at the interface, which explains the full transmission of the elastic waves between media I and II. At the free surface of the top Al plate (at $x_1 = 0$), the Rayleigh wave with the largest normal displacement (more than 2.5 nm in this simulation; see the color bar) is visible. In the bulk of the bilayer, the fastest wave (in red), which is reflected at the free surface of the lower Al plate (at $x_1 = 4.6$ mm), corresponds to the longitudinal wave. The slowest bulk wave is the transverse wave (in blue). The head wave is also simulated and corresponds to the plane wave that is generated at the critical angle $\theta_{crit} = \arcsin(\sqrt{C_{66}/C_{11}}) = 29.4°$, with the elastic coefficients C_{11} and C_{66} given in Table I.

In Fig. 5(b), three sublayers are inserted between the two Al plates: two distributions of normal and transverse interfacial stiffnesses equal to $K_{N_1} = K_{T_1} = \infty$ kN mm^{-3}, a 0.1 mm-thick epoxy layer, and two other interfacial stiffness distributions equal to $K_{N_2} = K_{T_2} = \infty$ kN mm^{-3}. The epoxy layer is assumed to be isotropic with a density of 2.1 10^3 kg m^{-3} and elastic coefficients $C_{11} = 4.2$ GPa and $C_{12} = 3.3$ GPa. Contrary to the bilayer Al/Al in Fig. 5(a), elastic waves are transmitted but also reflected by the epoxy layer.

This second example demonstrates the opportunities of the proposed model to predict/interpret the effect of imperfect bonding (by modifying the values of interfacial stiffnesses) on the detectable elastic waves in a bonded
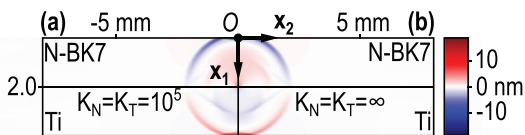
J. Acoust. Soc. Am. **150** (3), September 2021

Hodé *et al.* 2073

FIG. 6. (Color online) Normal displacements $u_1(x_1, x_2, t)$ simulated at $t = 0.35$ μs in a bilayer glass (2 mm)/Ti (2 mm) with interfacial stiffnesses equal to: (a) $K_N = K_T = 10^5$ kN mm^{-3} and (b) $K_N = K_T = \infty$ kN mm^{-3}. See the supplementary material (Ref. 23) for the animations.

multilayer structure. Possible applications of this semi-analytic model could be the simulation of laser-generated ultrasounds in structural bonding.[31] Indeed, quantifying the mechanical strength of bonds is a major issue in aeronautics. These simulations could allow understanding of the influence of a weak bond on the detected ultrasonic signature. These fast and accurate simulations could enable the resolution of inverse problems requiring the optimization of various key parameters related to the mechanical strength of adhesive bonding. Moreover, the transfer matrix formalism, used in this semi-analytic model, provides an easy way to extend the calculations to a structure with several sublayers between media I and II.

C. Bilayer with the heat source at the interface

The third example, in Fig. 6, is about a bilayer structure composed of a 2 mm-thick glass plate (SCHOTT N-BK7®) perfectly coupled to a 2.0 mm-thick titanium plate of ortho-tropic mechanical properties. To ensure the continuity of displacements and stresses at the interface, two distributions of normal and transverse interfacial stiffnesses are added and equal to $K_N = K_T = 10^5$ kN mm^{-3} in Fig. 6(a) and $K_N = K_T = \infty$ kN mm^{-3} in Fig. 6(b). The heat source is located at the interface between the two media because the incident electromagnetic wave is mainly absorbed in the titanium plate. Indeed, the complex part of the refractive index n'' is approximately 10^9 times higher for the titanium than for the glass plate (see Table I). Moreover, the normal displacement u_1 is similar in the two cases presented in Fig. 6(a) and 6(b) because large values of interfacial stiff-nesses ($K_N = K_T = 10^5$ kN mm^{-3}) are sufficient to ensure a perfect continuity of displacements and stresses at the inter-face between the two media. Furthermore, longitudinal bulk waves are mainly generated in the x_1-direction and the sign of the normal displacement is positive (negative) in the tita-nium (glass) plate. Transverse bulk waves and head waves are clearly visible (in blue) in the titanium plate.

This third example illustrates the fact that this model can be used to simulate a thermoelastic source at the inter-face between two media and not only at the upper surface of medium I, as previously shown in the first and second examples.

VII. CONCLUSION

Laser-generated ultrasounds are simulated in a multi-layer structure using a semi-analytic approach detailed in this paper. Electromagnetic, thermal, and elastodynamic problems are successively solved to obtain the displacement fields in the upper and lower media of the structure. A tilted laser line source, of infinite length in the x_3-axis, is consid-ered. The optical transmission and reflection of the incident laser beam are calculated to obtain the power densities dissi-pated into heat and used as source terms for solving the heat diffusion problem. The amplitudes of the thermal waves are obtained by considering conduction and convection phenomena. Then, analytic solutions of the displacement field because of the thermal expansion are determined in the Fourier domain. Finally, a double numerical inverse Fourier transform in space and time is performed to find the dis-placement field in the time domain.

In this 2D model, layered plates with parallel surfaces are considered, and it is assumed that the generation of ultra-sounds occurs only in the upper and lower media, i.e., the generation of ultrasounds in the sublayers should be negligi-ble. Therefore, the sublayers are accounted for in this semi-analytic model through the transfer matrix formalism. The model has been applied to three different cases showing just a glance of the possibilities such a model provides for fore-casting, designing, or else analyzing the elastic waves gener-ated and detected by lasers in multilayer structures. Note that this model, as long as the thermoelastic process of ultra-sound generation is at major play (i.e., the ablation regime and/or the plastic regime are not reached), is not limited to millimetric-in-thickness structure nor to the MHz frequency range. In addition, it can be extended to a 3D geometry to simulate ultrasound generation with thermoelastic sources that are no longer assumed to be of infinite length in the x_3-direction. This will obviously make the formulas presented in this paper more complex (the wavenumber k_3 must be added) and will necessarily increase the calculation time, which is about 1 min 37 s $\pm$ 6 s for a 2D geometry at a given x_1 position. However, this approach could be of real interest for simulating laser-generated ultrasounds in multilayer structures with thermoelastic sources of complex 3D shape.

[1]V. Gusev and A. Karabutov, *Laser Optoacoustics* (American Institute of Physics, New York, 1993).
[2]D. Royer and E. Dieulesaint, *Elastic Waves in Solids II: Generation, Acousto-Optic Interaction, Applications*, Advanced Texts in Physics, 1st ed. (Springer, Berlin Heidelberg, 2000).
[3]R. M. White, "Generation of elastic waves by transient surface heating," J. Appl. Phys. **34**(12), 3559–3567 (1963).
[4]C. B. Scruby, R. J. Dewhurst, D. A. Hutchins, and S. B. Palmer, "Quantitative studies of thermally generated elastic waves in laser-irradiated metals," J. Appl. Phys. **51**(12), 6210–6216 (1980).
[5]L. R. F. Rose, "Point-source representation for laser-generated ultra-sound," J. Acoust. Soc. Am. **75**(3), 723–732 (1984).
[6]M. Dubois, F. Enguehard, and L. Bertrand, "Analytical one-dimensional model to study the ultrasonic precursor generated by a laser," Phys. Rev. E **50**(2), 1548–1551 (1994).
[7]R. Coulette, E. Lafond, M.-H. Nadal, C. Gondard, F. Lepoutre, and O. Pétillon, "Laser-generated ultrasound applied to two layered materials characterization: Semi-analytical model and experimental validation," Ultrasonics **36**(1-5), 239–243 (1998).
[8]T. W. Murray, S. Krishnaswamy, and J. D. Achenbach, "Laser generation of ultrasound in films and coatings," Appl. Phys. Lett. **74**(23), 3561–3563 (1999).

2074   J. Acoust. Soc. Am. **150** (3), September 2021

Hodé *et al.*

[9] A. Cheng, T. W. Murray, and J. D. Achenbach, "Simulation of laser-generated ultrasonic waves in layered plates," J. Acoust. Soc. Am. **110**(2), 848–855 (2001).

[10] W. T. Thomson, "Transmission of elastic waves through a stratified solid medium," J. Appl. Phys. **21**(2), 89–93 (1950).

[11] B. Audoin and S. Guilbaud, "Acoustic waves generated by a line source in a viscoelastic anisotropic medium," Appl. Phys. Lett. **72**(7), 774–776 (1998).

[12] H. Meri, "Rayonnement d'ultrasons générés par laser dans les matériaux anisotropes: Effets de la pénétration optique, de la diffusion de la chaleur et de la diffusion de la densité électronique," Université Bordeaux I, 2004, Ph.D. thesis, www.theses.fr/2004BOR12842.

[13] M. Perton, "Ultrasounds radiated by a laser point source in transverse isotropic media. Applications to the stiffness tensor measurement of cylinders and thin layers," Université Bordeaux I, 2006, Ph.D. thesis, tel.archives-ouvertes.fr/tel-00179548.

[14] S. Raetz, "Development of numerical methods for the imaging of optoacoustic sources in solid media," Université Bordeaux I, 2012, Ph.D. thesis, www.theses.fr/2012BOR14624.

[15] Z. Shen, B. Xu, X. Ni, and J. Lu, "Numerical simulation of laser-generated ultrasonic waves in layered plates," J. Phys. D: Appl. Phys. **37**(17), 2364–2370 (2004).

[16] V. Dimitriou, E. Kaselouris, Y. Orphanos, M. Bakarezos, N. Vainos, M. Tatarakis, and N. A. Papadogiannis, "Three dimensional transient behavior of thin films surface under pulsed laser excitation," Appl. Phys. Lett. **103**(11), 114104 (2013).

[17] G. Yan, S. Raetz, N. Chigarev, J. Blondeau, V. E. Gusev, and V. Tournat, "Cumulative fatigue damage in thin aluminum films evaluated non-destructively with lasers via zero-group-velocity Lamb modes," NDT E Int. **116**, 102323 (2020).

[18] I. A. Veres, T. Berer, and P. Burgholzer, "Numerical modeling of thermoelastic generation of ultrasound by laser irradiation in the coupled thermoelasticity," Ultrasonics **53**(1), 141–149 (2013).

[19] P. Pyzik, A. Ziaja-Sujdak, J. Spytek, M. O'Donnell, I. Pelivanov, and L. Ambrozinski, "Detection of disbonds in adhesively bonded aluminum plates using laser-generated shear acoustic waves," Photoacoustics **21**, 100226 (2021).

[20] M. Born and E. Wolf, *Principles of Optics: Electromagnetic Theory of Propagation, Interference and Diffraction of Light* 7th ed. (expanded) (Cambridge University Press, Cambridge, 1999).

[21] J. Singh, *ed., Optical Properties of Materials and Their Applications* (John Wiley & Sons, Hoboken, 2019).

[22] L. M. Brekhovskikh, *Waves in Layered Media*, 2nd ed., Applied Mathematics and Mechanics Vol. 16 (Academic Press, Elsevier, New York, 1980).

[23] See supplementary material at https://www.scitation.org/doi/suppl/10.1121/10.0005974 for the definition of the transfer matrix $[L^{EM}]$; detailed expressions of the coefficients A_{ij}^T and B_i^T; and the expression of the transfer matrix $[L^M]$.

[24] S. Raetz, T. Dehoux, and B. Audoin, "Effect of laser beam incidence angle on the thermoelastic generation in semi-transparent materials," J. Acoust. Soc. Am. **130**(6), 3691–3697 (2011).

[25] D. W. Hahn and M. N. Özişik, *Heat Conduction*, 3rd ed. (John Wiley and Sons, Hoboken, 2012).

[26] M. Bouchon and K. Aid, "Near-field of a seismic source in a layered medium with irregular interfaces," Geophys. J. Int. **50**, 669–684 (1977).

[27] R. L. Weaver, W. Sachse, and L. Niu, "Transient ultrasonic waves in a viscoelastic plate: Applications to materials characterization," J. Acoust. Soc. Am. **85**(6), 2262–2267 (1989).

[28] R. L. Weaver, W. Sachse, and K. Y. Kim, "Transient elastic waves in a transversely isotropic plate," J. Appl. Mech. **63**(2), 337–346 (1996).

[29] J. A. Brammer and C. M. Percival, "Elevated-temperature elastic moduli of 2024 aluminum obtained by a laser-pulse technique," Exp. Mech. **10**(6), 245–250 (1970).

[30] M. N. Polyanskiy, "Refractive index database," https://refractiveindex.info, accessed on 2020-06-19.

[31] R. Hodé, S. Raetz, N. Chigarev, J. Blondeau, N. Cuvillier, V. Gusev, M. Ducousso, and V. Tournat, "Laser ultrasonics in a multilayer structure: Plane wave synthesis and inverse problem for nondestructive evaluation of adhesive bondings," J. Acoust. Soc. Am. **150**, 2076–2087 (2021).

J. Acoust. Soc. Am. **150** (3), September 2021

Hodé *et al.* 2075